Journal of Materials Chemistry C

ROYAL SOCIETY OF CHEMISTRY

PAPER

View Article Online
View Journal | View Issue

Cite this: J. Mater. Chem. C, 2025, 13, 13752

Multifunctional benzonitrile derivatives with TADF and mechanofluorochromic properties and their application in OLEDs†

Antonio Maggiore, *[ab] Yangyang Qu,[a] Gilles Clavier,[a] Marco Colella,[c] Andrew Danos,[cd] Andrew Monkman,[c] Regis Guillot,[e] Marco Pugliese,[b] C. Tania Prontera,[b] Roberto Giannuzzi,[b] Fabrizio Mariano,[b] Sonia Carallo,[b] Gianluca Accorsi,[b] Vincenzo Maiorano,[b] Pierre Audebert,[a] Remì Metivier[a] and Fabien Miomandre[a]

Received 10th October 2024,
Accepted 26th April 2025

DOI: 10.1039/d4tc04347b

rsc.li/materials-c

In this study, we explore the solid-state photophysical properties of four donor–acceptor–donor′ (D–A–D′) fluorinated benzonitrile compounds, featuring combinations of phenoxazine and carbazole donor units. We have previously shown that these compounds exhibit dual charge transfer thermally activated delayed fluorescence (CT-TADF) emission in solution; here we investigate the steady-state and time-resolved photophysical properties in the solid state. Initial photophysical characterizations were performed in polymethyl methacrylate (PMMA) polymer films, followed by detailed studies of the supramolecular packing in neat films under various preparation conditions, including solvent exposure and thermal treatments. Different polymorphs and amorphous phases were obtained, revealing that the dual TADF emission could be maintained to some extent in the solid-state. Mechanical stress and solvent vapour exposure induced mechanochromic luminescence (MCL), with emission changes correlating to the supramolecular structures. OLED devices were also fabricated, demonstrating similar tuneable emission properties based on preparation techniques. This work highlights the potential of this class of materials towards advanced optoelectronic applications with tuneable and stimuli-responsive emission characteristics.

1. Introduction

Organic semiconductor materials that efficiently harvest otherwise non-emissive triplet excitons are crucial for optoelectronic devices,[1,2] such as organic light-emitting diodes (OLEDs) and organic photovoltaics (OPVs).[3] To date, several strategies have been proposed to harvest triplet excitons, with the most promising based on thermally activated delayed fluorescence (TADF) emitters.[4–7] These fully organic materials have attracted tremendous attention as they allow for the replacement of rare and/or toxic organometallic complexes traditionally used as phosphorescent emitting layers in OLED devices. Triplet harvesting in TADF materials is achieved by molecular designs that result in a very small singlet–triplet energy gap (ΔE_{S-T}), typically less than 0.1 eV and comparable to ambient thermal energy. This small gap allows triplet excitons to be upconverted back to the singlet *via* the reverse intersystem crossing (RISC) process, enabling emission. To reduce ΔE_{S-T}, it is necessary to minimize the spatial overlap between the highest occupied molecular orbital (HOMO) and the lowest unoccupied molecular orbital (LUMO).[7] The most common strategy towards this end is to use donor–acceptor (D–A) or donor–acceptor–donor (D–A–D) designs, which promote the formation of strong charge transfer (CT) states.[8] The HOMO/LUMO spatial separation can be further increased by using a phenyl linker as the spacer, or by tilting the D–A torsional angle to a nearly orthogonal configuration.[9–11] This pre-twisted D–A configuration also helps to avoid tight packing and detrimental strong π–π interactions that favor non-radiative deactivation channels in the solid state.[12,13] In addition, D–A and D–A–D luminescent organic materials, thanks to the presence of strong CT states,

[a] Université Paris-Saclay, ENS Paris-Saclay, CNRS, PPSM, Gif-sur-Yvette, 91190, France
[b] CNR-NANOTEC – Institute of Nanotechnology, c/o Campus Ecoteckne, Via Monteroni, Lecce, 73100, Italy. E-mail: antonio.maggiore@cnr.it
[c] Department of Physics, University of Durham, South Road, Durham, DH1 3LE, UK
[d] School of Physical and Chemical Sciences, Queen Mary University of London, London, E1 4NS, UK
[e] Université Paris-Saclay, CNRS, Institut de chimie moléculaire et des matériaux d'Orsay, Orsay, 91405, France

† Electronic supplementary information (ESI) available. See DOI: https://doi.org/10.1039/d4tc04347b

show a strong ability to change their optical output in response to environmental changes (*e.g.* solvent polarity, medium stiffness, *etc.*).[14–17]

It has also been shown that D–A and D–A–D materials in the condensed phase can be highly sensitive to external stimuli such as grinding or pressing, exhibiting mechanochromic luminescence (MCL) behaviour, as well as heating and solvent exposure,[18,19] all of which impact emission colour either by enacting conformational changes in the molecules or by altering intermolecular interactions between neighbouring molecules.[20–23] Mechanochromic luminescence typically starts from a crystalline or aggregated phase that switches to another crystalline or amorphous phase after mechanical stress, with an accompanying change in the emission spectrum, this phenomenon being allowed by the polymorphism of the material. The search for polymorphic crystal forms of such emitters is widely investigated as it enables interesting properties and applications, especially in optoelectronics.[24–27] The high sensitivity of some D–A materials to external stimuli, together with their ability to resist aggregation caused quenching (ACQ) phenomena, is driving research to develop new D–A materials with MCL properties,[28–30] particularly for sensor development.

In the present work, we investigate the solid-state photophysical properties of a series of four donor–acceptor–donor′ (D–A–D′) fluorinated benzonitrile (BzN, A) compounds (Fig. 1a) substituted with mixed phenoxazine (PhOx) and carbazole (Cz) donor units (D and D′). We have previously shown that these compounds exhibit dual CT-TADF emission in solution, from excited states involving Cz and PhOx.[31] In this study, we have investigated in detail the steady-state and time-resolved photophysical properties in polymethylmethacrylate (PMMA) rigid films, as well as in the non-doped condensed phase. We have specifically studied the supramolecular packing obtained in neat films by varying the sample preparation conditions (*e.g.* type of solvent, solvent saturation conditions and temperature; see the ESI† for more details). This allows us to obtain different polymorphs or amorphous phases with various MCL properties that also translate to OLED emission in non-doped emissive layers.

2. Results and discussion

2.1. Steady-state PL of the isolated molecule in dilute solution and polymer matrix

The steady state emission properties of isolated molecules **4–7**, both in solution and within a rigid polymer matrix, have been previously reported.[31] We retain the molecular naming conventions from this previous work to enable straightforward comparisons here, and briefly summarize the PL in cyclohexane (CH) and in the rigid polymer environment (PMMA) (Fig. 1). In solution, dual emission is evident when the molecule is excited at the locally excited (LE) absorption band (higher energy) (Fig. 1b). However, when excited at the lower energy CT absorption band (Fig. S12, ESI†), only a single emission band remains (inset, Fig. 1b). In contrast, in PMMA, the higher energy band appears weak and diminishes further with an increasing number of carbazole (Cz) units. As discussed previously,[31] for compounds **4** and **5**, the higher energy emission is attributed to the sum of both LE from PhOx and CT involving Cz contributions. For compounds **6** and **7** it is attributed exclusively to Cz CT. The lower energy band for all

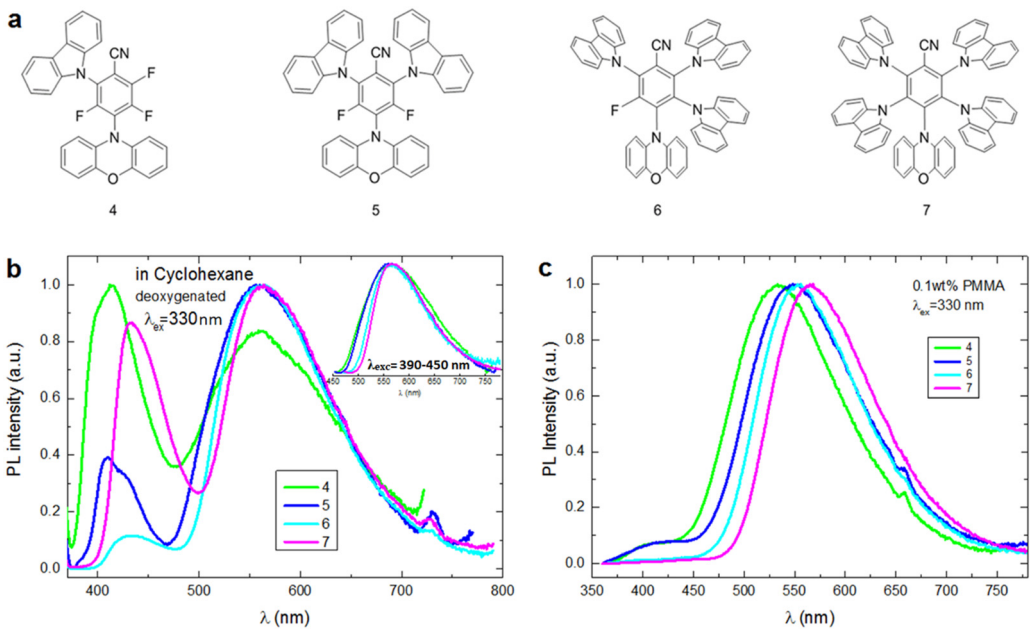

Fig. 1 (a) Molecular structures of the molecules studied. (b) Normalized photoluminescence spectra of **4–7** in cyclohexane (10^{-5} M). Inset: Normalized photoluminescence spectra of **4–7** in cyclohexane (10^{-5} M) excited on the lower energy CT band, λ_{exc} = 390–450 nm. (c) Normalized photoluminescence spectra of **4–7** in PMMA.

compounds is assigned to the CT state involving phenoxazine (PhOx CT).[31] From the inset of Fig. 1b, we can observe a slight red shift of the emission, particularly at the onset, with an increasing number of carbazole units. This behaviour is more pronounced in PMMA (Fig. 1c), indicating that the number of Cz units also influences the CT involving phenoxazine. The different behaviour observed in the solid environment is likely due to the restricted rotation of carbazole in the solid state compared to the solution, which prevents the stabilization of the Cz CT state.[32] As a result, most of the energy is directed towards the PhOx CT through internal conversion processes.

2.2. Study in the condensed phase

Here we report the photophysical properties and XRD analysis of the condensed phase samples. We begin by describing the various sample preparation techniques used to control the supramolecular arrangement of the studied materials. All samples with the corresponding preparation techniques are summarized in Table 1.

To prepare the different neat (non-doped) films, we varied the chemical and physical processing conditions such as solvent polarity, temperature and evaporation rate (see the ESI† for more details). Fast solvent evaporation (conducted under a hood) resulted in amorphous films, while slower, controlled evaporation (achieved by saturating the evaporation chamber with the solvent) generally resulted in more ordered or crystalline phases. Specifically:

– Solvent vapour annealing (SVA) is a slow evaporation process where the solvent vapor environment promotes molecular mobility, favouring self-assembly and crystallization.[33] The samples obtained by solvent vapour annealing (using as a solvent toluene into a hexane saturated chamber, see the ESI† for details) of particular emitter "X" are labelled as "**XfSVA**", (f = from).

Table 1 Samples obtained using the different preparation techniques described above

Molecule	Sample name	Preparation technique
4	**4fDCM**	Drop casting from DCM
	4fSVA	Solvent vapour annealing
	4fDCM150	Drop casting from DCM + 150 °C
	4fTOL	Drop casting from toluene
5	**5fDCM**	Drop casting from DCM
	5fSVA	Solvent vapour annealing
	5fDCM150	Drop casting from DCM + 150 °C
	5fTOL	Drop casting from toluene
6	**6fDCM**	Drop casting from DCM
	6fSVA	Solvent vapour annealing
	6fDCM150	Drop casting from DCM + 150 °C
	6FDCM200	Drop casting from DCM + 200 °C
	6fTOL	Drop casting from toluene
7	**7fDCM**	Drop casting from DCM
	7fSVA	Solvent vapour annealing
	7fDCM150	Drop casting from DCM + 150 °C
	7fTOL	Drop casting from Toluene

– Dropping the solution directly onto the substrate enables us to control the assembly by selecting appropriate solvents. We used two different solvents: DCM (dichloromethane), which has a low boiling point and fast evaporation properties, favouring an amorphous phase, and toluene, which has a high boiling point and high viscosity, favouring high-order molecular self-assembly. The samples obtained by drop casting with DCM are labelled with postscript **fDCM**, and those from toluene with **fTOL**.

– In addition, we also used thermal annealing, which facilitates molecular diffusion and nucleation, leading to crystalline phases following initial deposition. This was achieved by heating the drop cast samples from the DCM solution at 150 °C or 200 °C for 15 minutes. The samples obtained by thermally annealing are labelled as **fDCM150** (T = 150 °C) and **fDCM200** (T = 200 °C).

Images of all prepared samples are shown in the ESI† (Fig. S1–S4).

2.2.1. XRD analysis, optical microscopy, and scanning electron microscopy (SEM). The crystallinity of the thin films was evaluated by powder X-ray diffraction (XRD) (Fig. 2), while their surface morphology was investigated through optical microscopy and scanning electron microscopy (SEM) (Fig. 3 and Fig. S11, top and bottom panels, respectively, ESI†). These complementary techniques provide insight into both molecular packing and surface organization.

All films prepared *via* solvent vapor annealing (**fSVA**) and thermal annealing at 150–200 °C display distinct diffraction peaks, confirming the presence of crystalline phases. Similarly, all **fTOL** samples exhibit crystalline features, with the exception of **5fTOL**. In contrast, **fDCM** films are X-ray amorphous, consistent with the rapid solvent evaporation hindering molecular organization. Notably, variations in XRD patterns across different processing methods for the same molecule indicate polymorphism or variations in molecular packing driven by distinct crystallization dynamics. Single-crystal X-ray diffraction was also performed on crystals obtained from the initial powders (used for the MCL study in Section 5). For molecule **5**, the unit cell contains two distinct molecules and one solvent molecule with different donor–acceptor (D–A) angles, consistent with the presence of multiple charge-transfer (CT) states (Table S1, ESI†). Two polymorphic forms were identified for molecule **6**, one solvent-free and one solvated (**6** and **6+solv**), supporting the hypothesis that polymorphism plays a key role in modulating solid-state emission properties (Table S1, ESI†). Molecular packing in the single crystals of compounds **4–7** is illustrated in Fig. S5–S10 (ESI†). Key intermolecular interactions include C–H···π, C–H···N, C–F···H, C–H···O, and C–F···C. Notably, π–π stacking is observed only for compound **5** (offset stacking between two carbazole units with a π–π distance of 3.702 Å; Fig. S5b and S7, ESI†) and for **6+solv** (offset, head-to-tail stacking between carbazoles with a distance of 3.867 Å; Fig. S5d and S9, ESI†). The presence of multiple donor groups and relatively weak directional interactions appears to facilitate conformational adaptability and structural rearrangement, consistent with the MCL behaviour observed in these systems.[34–36]

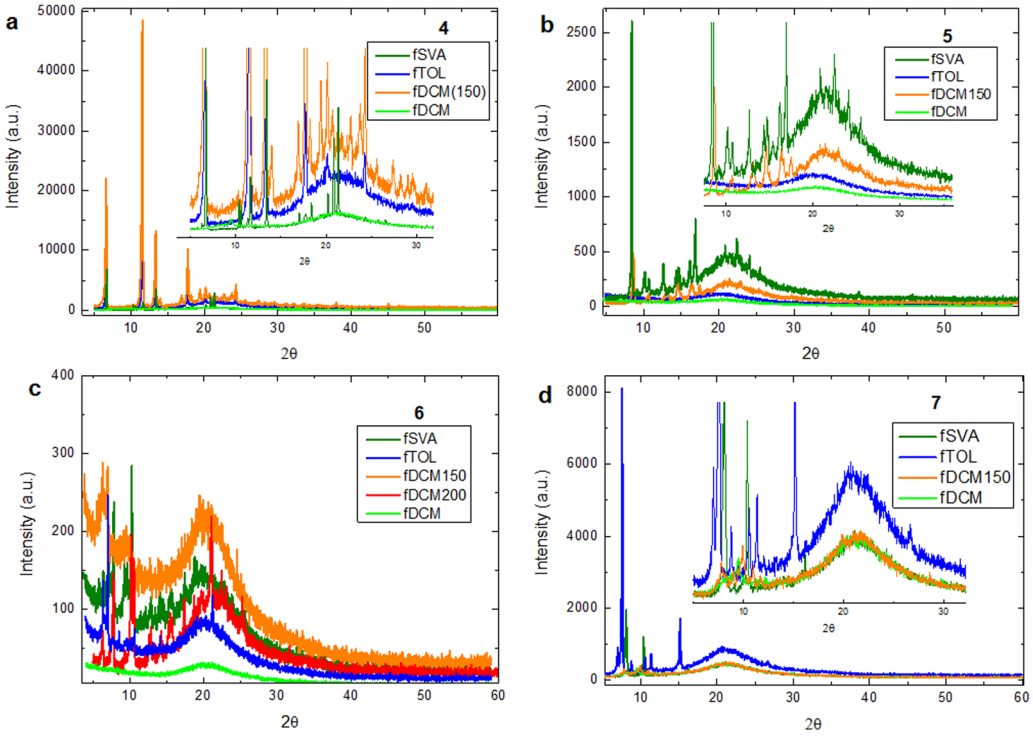

Fig. 2 Powder XRD patterns of different forms of the reported molecules: (a) molecule **4**, (b) molecule **5**, (c) molecule **6**, and (d) molecule **7**.

Optical and SEM images (Fig. 3 and Fig. S11, ESI†) corroborate the structural data obtained from XRD. Films obtained *via* **fSVA** show well-defined surface textures, with crystalline domains clearly observable under both optical and electron microscopy. The **fTOL** samples, excluding **5fTOL**, also display heterogeneous morphologies, characterized by visible crystalline regions. For instance, **4fTOL** features faceted multidomain sheets, while **6fTOL** exhibits rectangular, flat crystalline domains. In **7fTOL**, SEM reveals micrometric, filament-like aggregates not easily detected in optical images. In contrast, **fDCM** samples appear smooth and homogeneous in both optical and SEM analysis, reflecting their amorphous nature as confirmed by XRD. Similarly, **5fTOL** presents a featureless morphology, consistent with its amorphous character. Upon thermal annealing of **fDCM** films, the formation of crystalline domains becomes evident. Optical and SEM images reveal the emergence of textured crystalline regions in **4fDCM150**, **6fDCM150**, **6fDCM200**, and **7fDCM150**. Interestingly, while **5fDCM150** appears featureless in optical microscopy, SEM at 20 μm resolution reveals branched crystalline domains. At higher magnification (4 μm), these appear as elongated, bar-like or rod-like structures (Fig. S11, ESI†).

Comparative analysis of the crystalline morphologies across different preparation methods provides further insight highlighting the sensitivity of molecular organization to processing conditions. Molecule **4** forms elongated, interconnected needle-like crystalline domains in **fSVA**. In **4fTOL**, the crystals appear as large, flat, multifaceted domains with irregular polygonal boundaries. **4fDCM150** exhibits smaller, elongated rectangular flat domains. Molecule **5** forms elongated hexagonal platelets domains in **fSVA**, characterized by sharp edges and well-defined facets. **5fDCM150** displays a heterogeneous morphology; high-magnification SEM reveals small crystallites with bar-like or branched structures radiating from localized nucleation points (4 μm scale, Fig. S11, ESI†). For molecule **6**, **fSVA** induces elongated spear-like crystallites. **6fTOL** shows smaller rectangular faceted crystalline domains, while **6fDCM150** presents a polycrystalline mosaic texture. Upon annealing at 200 °C (**6fDCM200**), a clear morphological transition occurs, showing interconnected crystalline areas with petal-like features. Molecule **7** displays elongated hexagonal crystalline facets in **fSVA**. SEM images of **7fTOL** reveal fibrous or needle-like crystalline structures. In **7fDCM150**, SEM analysis shows parallelogram-shaped crystalline domains.

The combined XRD and microscopy analyses clearly demonstrate that the processing method strongly influences the crystallinity, molecular packing, and surface morphology of **4–7** thin films. The ability of each molecule to adopt multiple packing arrangements under different conditions is closely related to its polymorphic behaviour and is directly linked to the solid-state photophysical properties explored in subsequent sections.

2.2.2. Steady state photophysical study in the condensed phase (neat film and crystalline powder). The steady-state PL emission spectra of the various films and powders are depicted in Fig. 4, while the photophysical properties are summarized in Table 2 (additional details are presented in the ESI†). All crystalline samples (which mainly include those with acronyms **fSVA**, **fTOL** and **fDCM150/fDCM200**) exhibit significantly narrowed emission compared to both their amorphous forms

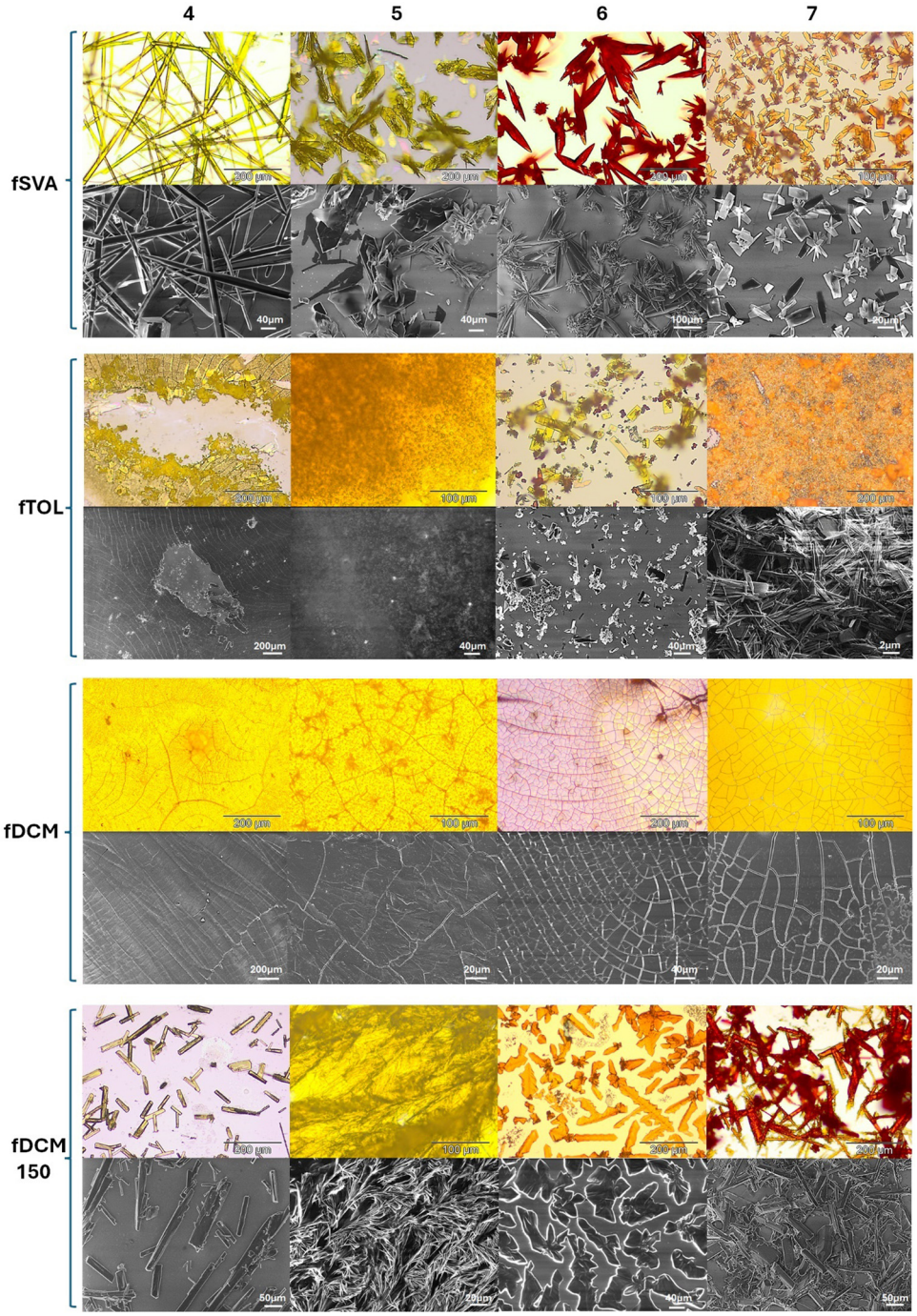

Fig. 3 Surface morphology of samples **4–7** prepared using the different processing methods (**fDCM**, **fTOL**, **fSVA**, and **fDCM150**). Top panels (colour images) show optical microscopy photographs. Bottom panels (black and white images) display the corresponding scanning electron microscopy (SEM) images. The images revealing microscale surface features and morphological variations induced by the preparation methods. Scale bars are included in all optical and SEM images.

(Fig. 4 and Table 2) and in PMMA (Fig. S12, ESI†). This suggest that the highly ordered packing typical of crystals reduces the number or freedom of molecular conformations, which are otherwise allowed in PMMA and amorphous samples. Furthermore, all different solid forms of compounds **4–7** show red-shifted emission compared to the isolated molecules in PMMA (Table 2 *vs.* Table S2, ESI†). This suggests that aggregation shifts the optical gap downwards due to the properties of the solid phase (D–A torsion angle, polarity and dielectric constant).[37,38] Compared to their amorphous form, a strong hypsochromic shift is observed in the crystalline forms of **4**, **5** and **7**, while for compound **6** only **6fTOL** and **6fDCM150** show a hypsochromic shift (**6fSVA** shows a red shift). The higher PLQY observed for crystalline samples **4**, **5** and **7** and **6fDCM150**

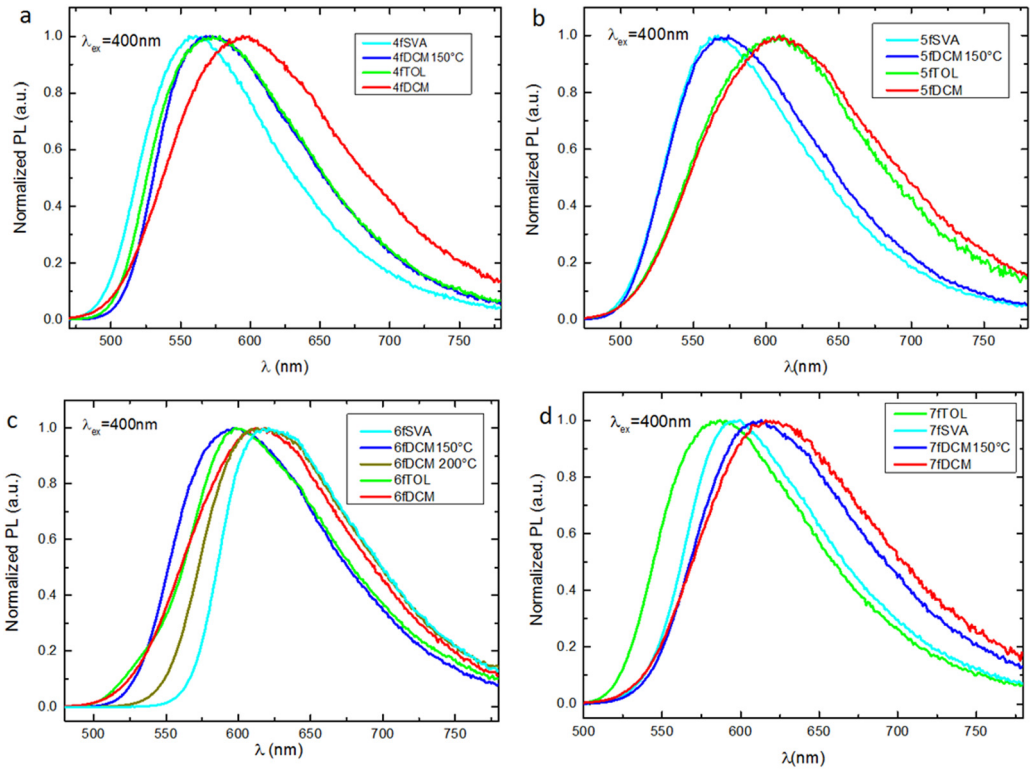

Fig. 4 Normalized fluorescence spectra (λ_{exc} = 400 nm) of the different solid forms obtained for (a) molecule **4**, (b) molecule **5**, (c) molecule **6**, and (d) molecule **7**.

Table 2 Summary of steady state photophysical properties of the different solid samples

Comp.	QY (%) air	λ_{PL} (nm) Std. state	FWHM (nm)	Emission onset (eV)	Excitation onset (eV)
4SVA	9.0	561	112	2.51	2.36
4fDCM150	3.3	573	124	2.43	2.32
4fTOL	2.7	573	128	2.47	2.38
4fDCM	1.0	594	141	2.46	2.31
5SVA	7.8	567	112	2.47	2.36
5fDCM150	4.1	574	121	2.47	2.37
5fTOL	1.1	610	140	2.44	2.35
5fDCM	1.0	612	149	2.44	2.34
6SVA	2.4	626	113	2.19	2.07
6fDCM150	7.3	598	123	2.35	2.31
6fDCM200	2.9	621	125	2.25	2.16
6fTOL	2.6	598	116	2.33	2.15
6fDCM	2.3	612	132	2.36	2.35
7SVA	8.5	600	104	2.29	2.16
7fDCM150	2.8	613	124	2.29	2.13
7fTOL	9.1	585	115	2.38	2.25
7fDCM	1.8	620	131	2.31	2.21

compared to their amorphous forms indicates a crystallization-induced enhanced emission (CIEE). Samples **4**, **5** and **7** also show higher QYs for crystalline films obtained by solvent vapour annealing, probably due to their higher crystalline quality. Fig. S13a (ESI†) shows the emission spectra of all crystalline forms, where a progressive bathochromic shift in both maxima and onset can be observed with an increasing number of Cz units (except for one of the polymorphs of compounds **6** and **7**, which does not follow this trend). Interestingly, a progressive bathochromic shift is also observed in the amorphous samples (Fig. S13b, ESI†) with increasing number of Cz units, in agreement with previous observations for molecules dispersed in PMMA.

Notably, each polymorph of compounds **6** and **7** (isolated in the XRD analysis) shows different photophysical behaviour. The emission at the highest energy is observed for **6fDCM150**, which also exhibits CIEE properties (Table 2 and Fig. S13a, ESI†). In contrast the emission at lowest energy is detected for

6fSVA, which has the lowest QY in agreement with the energy gap law (Table 2 and Fig. S13a, ESI†). Interestingly, the crystalline **6fSVA** film shows a bathochromic shift relative to the amorphous **6fDCM** (Fig. S13a and b, ESI†), indicating that this molecular packing strongly stabilizes the CT state, leading to increased non-radiative deactivation paths. Conversely, **7fTOL** shows a hypsochromic shift with higher PLQY relative to **7fSVA** (Table 2 and Fig. S13a, ESI†). Looking at the different solid samples obtained from the same molecule, it can be seen that the bluer shifted the emission, the higher the QY (Table 2 and Fig. S13, ESI†). This behaviour is also valid for the polymorphs in **7fTOL**/**7fSVA** and **6fDCM150**/**6fSVA**.

Fig. S14 (ESI†) shows the absorption and excitation (PE) spectra of **4–7** in PMMA, and their good match indicates that all transitions involved in the absorption process contribute to the emission output. As previously discussed for the absorption in PMMA, the bands at lower energy are assigned to the CT transitions of PhOx–BzN (CT1) and Cz–BzN (CT2) moieties. Fig. S15 (ESI†) instead shows the PE spectra of all neat films, compared as well to PMMA, while those in Table S3 (ESI†) are reported for their peak maxima (λ_{max}) and the onset for the lower energy bands. We can observe that for all molecules the higher energy peaks (between 363 and 367 nm), are intense and match with both the absorption and PE spectra of **4–7** in PMMA (Fig. S14, ESI†), and thus are assigned to the locally excited state of the donors. On the other hand, in neat films the CT1 and CT2 bands are strongly red-shifted and in most cases are also more intense compared to the isolated molecules in PMMA (Fig. S15 and Table S3, ESI†). Since no short distance π–π interactions were found (only long-distance π–π interactions between two carbazoles were found in **5** and **6+solv** crystals Fig. S7 and S9, ESI†), the formation of aggregate emissive species is not orderly in these films. Therefore, the strong red-shift in the CT transitions observed in PE spectra can be attributed to either the presence of different molecular conformations in the solid samples and/or to different polarity and dielectric constants in the solid phases. These factors can produce a redistribution of the electronic density of the molecules that stabilizes the CT states.

2.3. Time-resolved photophysical properties

2.3.1. Time-resolved photophysical properties of the isolated molecules in PMMA. In order to investigate their TADF properties and gain more insight into the nature of the double emission previously demonstrated in solution for these systems,[31] the time-resolved studies of **4–7** in PMMA were conducted at RT and 77 K. The time-resolved emission spectra for all the compounds at RT are shown in Fig. 5. For all molecules, the early emission features a shoulder or band at higher energy (450 nm) alongside the main band centered at 550 nm. The higher-energy shoulder can be attributed to both the initial locally excited (LE) state of the donors and/or the prompt charge-transfer (CT) emission from the higher-energy BzN–Cz pair, while the main band is assigned to the CT emission from the lower energy BzN–PhOx pair.[39] As the delay time increases, the higher-energy shoulder/band progressively disappears. After 100 ns, the delayed fluorescence (DF) emission arises solely from the ^{1}CT state involving the phenoxazine

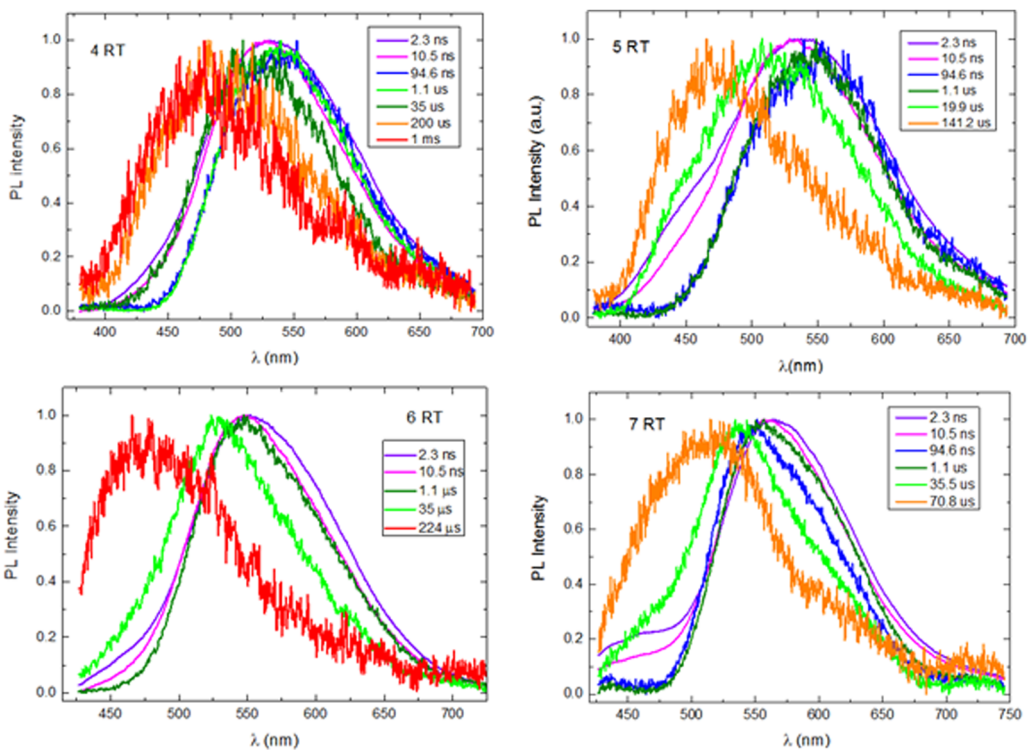

Fig. 5 Normalized time-resolved emission spectra of **4–7** in PMMA at room temperature (RT).

Table 3 Summary of time resolved photophysical properties

	$\lambda_{std.st.}$ (nm)	λ_{PF} (nm)	$S1_{onset}$ (eV)	τ_1 (ns)	τ_2 (μs)	τ_3 (μs)	τ_4 (μs)	$\tau_{DF,av}$	QY (%)	DF/PF
4fDCM	594	605	2.41	2.2	0.3	0.9	4.0	1.3	1.0	0.03
4fTOL	573	602	2.43	2.6	0.1	1.2	—	0.9	2.7	0.05
4fDCM150	573	560	2.43	4.0	1.4	—	—	1.4*	3.3	0.09
4fSVA	561	573	2.38	4.0	1.2	—	—	1.2*	9.0	0.08
5fDCM	612	600	2.36	2.2	0.2	0.8	3.7	1.4	1.0	0.17
5fTOL	610	585	2.40	2.0	0.1	0.6	2.6	1.2	1.1	0.07
5fDCM150	574	562	2.46	4.6	0.4	2.8	—	2.2	4.1	0.15
5fSVA	567	562	2.44	8.7	0.7	—	—	0.7*	7.8	0.22
6fDCM	612	609	2.28	3.1	0.2	1.3	4.4	1.3	2.3	0.05
6fDCM150	598	579	2.37	4.3	2.5	—	—	2.5*	7.3	0.06
6fDCM200	621	612	2.21	3.3	1.0	—	—	1.0*	2.9	0.04
6fSVA	626	614	2.19	3.1	1.1	—	—	1.1*	2.4	0.04
7fDCM	620	611	2.30	2.2	0.03	0.3	2.0	1.6	1.8	0.05
7fSVA	600	577	2.35	4.6	0.3	4.9	—	4.2	8.5	0.16
7fTOL	585	574	2.39	5.2	0.3	5.6	—	4.7	9.1	0.26

$\lambda_{std.st.}$ = emission maximum of steady-state fluorescence, λ_{PF} = emission maximum of prompt fluorescence, $S1_{onset}$ = onset energy of singlet, $\tau_{PF,av}$ = average decay time of PF, $\tau_{DF,av}$ = average decay time of DF, *: monoexponential, DF/PF= ratio between DF to PF emission.

(BzN–PhOx), which remains the dominant state up to 1–10 microseconds. With further delay, up to hundreds of microseconds, the emission shifts back to higher energies. This long-lived DF is attributed to the CT involving the carbazole, as indicated by the match with the PL profile [time delay (TD) = 10 μs] of Cz–BzN in PMMA (see Fig. S16, ESI†).

The decay profiles of all compounds at RT in PMMA are shown in Fig. S20 (ESI†), and the decay times of other films (decays in Fig. S22–S36, ESI†) are summarized in Table 3. The prompt fluorescence (PF) part of the decay (nanosecond domain) is fitted with a biexponential function, with the two components associated with PF emission from the ^{1}LE of PhOx and/or the ^{1}CT of BzN–Cz. Similarly, the long-lived component (DF domain) also shows biexponential behavior, but in this case, the two decay times can be attributed to DF arising from the two CT states associated with the PhOx–BzN and Cz–BzN moieties. The power law relationship between DF emission intensity and excitation dose with gradient close to 1 confirms a monomolecular process for all compounds, excluding TTA as the DF mechanism (Fig. S17, S37–S40, ESI†). Both the time-resolved PL emission and decay profiles at RT show that, similar to the solution phase, dual TADF emission channels are present in the solid-state environment. However, the higher energy DF (originating from the Cz–BzN branch) contributes negligibly to the total emission output.

Time-resolved emission was also collected at 77 K (Fig. S18, ESI†). Similar to RT, at initial times (nanosecond range), the time-resolved PL emission shows a shoulder/band at higher energy (450 nm) attributed to the PF of the ^{1}LE of PhOx and/or the ^{1}CT of BzN–Cz, and a main band at lower energy attributed to the ^{1}CT PF of the PhOx–BzN moieties. With increasing delay time, the emission progressively redshifts and after 100 ns the shoulder at 450 nm disappears, leaving only a DF emission from the ^{1}CT of the PhOx–BzN moiety. With further increasing the delay time, the emission progressively blue shifts and in some cases gains structural features, and since the late emission (TD = 70 ms) has an onset close to the phosphorescence of phenoxazine (Fig. S19, ESI†), it can be attributed to the emission from the phenoxazine fragment ^{3}LE.

In conclusion, the time-resolved study in polymer shows that the dual TADF emission previously shown in solution remains present in the solid state. However, the higher energy DF emission (originating from the Cz–BzN branch) contributes negligibly to the total emission.

2.3.1. Time-resolved photophysical properties of the neat films. Time-resolved measurements of compounds **4–7** in neat film were similarly carried out at room temperature (RT). The samples were prepared using the same deposition technique but with a different substrate (sapphire discs instead of quartz rectangles‡). The emission follows the same trend as the steady-state study (Fig. S21, ESI†), except for **4fTOL**, which shows the same emission as the amorphous **4fDCM**. All the time-resolved studies are reported in the ESI† (Fig. S22–S36), while the photophysical properties are summarized in Table 3.

From the time-resolved spectra, it is evident that all samples exhibit typical TADF behaviour. However, while the emission in crystalline samples remains unchanged at different delay times (**4fDCM150**, **4fSVA**, **5fDCM150**, **5fSVA**, **6fDCM150**, **6fDCM200**, **6fSVA**, **7fTOL**, **7fSVA**), the amorphous samples show slight spectral evolution over time (**4fDCM**, **4fTOL**, **5fDCM**, **5fTOL**, **6fDCM**, and **7fDCM**). Consequently, the amorphous films are fitted with bi- or multi-exponential curves, while the crystalline ones, with few exceptions, are fitted with mono-exponential curves. The laser fluency experiments reported in Fig. S37–S40 (ESI†) again show the expected linear dependence of the DF intensity on the laser power. Based on these observations, we can conclude that the dual emission observed in solution and in the polymer matrix is not as strongly maintained in the non-doped condensed phase. The double exponential decay observed in the amorphous samples is probably caused by the poor homogeneity of the films, which contain molecules with slightly different configurations. In contrast, the ordered

‡ To allow these smaller samples to fit into the cryostat.

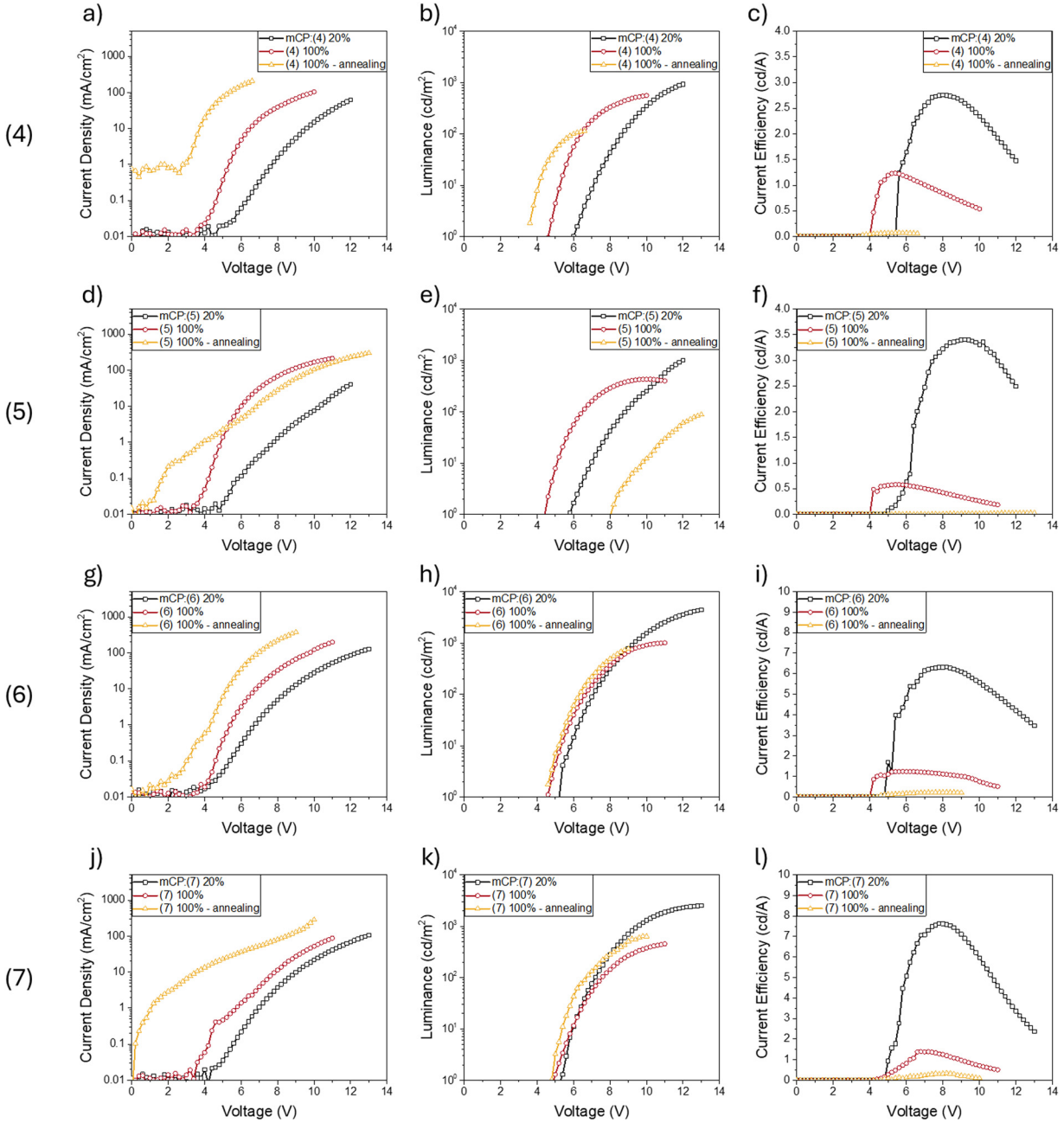

Fig. 6 Electroluminescent characteristics of OLEDs using **4**, **5**, **6** and **7** as the active layer, dispersed in an appropriate matrix (mCP) and in neat film (with or without annealing). Voltage *vs.* current density, voltage *vs.* luminance and voltage *vs.* efficiency for molecules **4** (a)–(c), **5** (d)–(f), **6** (g)–(i) and **7** (j)–(l).

packing of crystalline films allows only one molecular conformation to dominate.

2.4. OLED devices

To demonstrate the possibility of using this class of compound as emitting materials in an electroluminescent device, we fabricated OLEDs with the materials **4**, **5**, **6** and **7** as emitting layers (EMLs). The compounds were dispersed at 20% w/w in an appropriate host matrix (1,3-bis(*N*-carbazolyl)benzene, mCP), and the device's structure was as follow: ITO/Pedot:PSS (35 nm)/PVK (10 nm)/mCP:compound **4**–**7** 20% w/w (30 nm)/TPBI (50 nm)/LiF (1 nm)/Al (100 nm). We also fabricated OLEDs using thin neat films (100%) of the materials **4**, **5**, **6** and **7** as emitting layers (EMLs), testing the effect of annealing on the EMLs in order to evaluate how the supramolecular packing can influence the electroluminescence properties.

The results of electro-optical characterization of the OLEDs are shown in Fig. 6. As expected, devices using a host:guest system as EML perform better than the neat film case. In

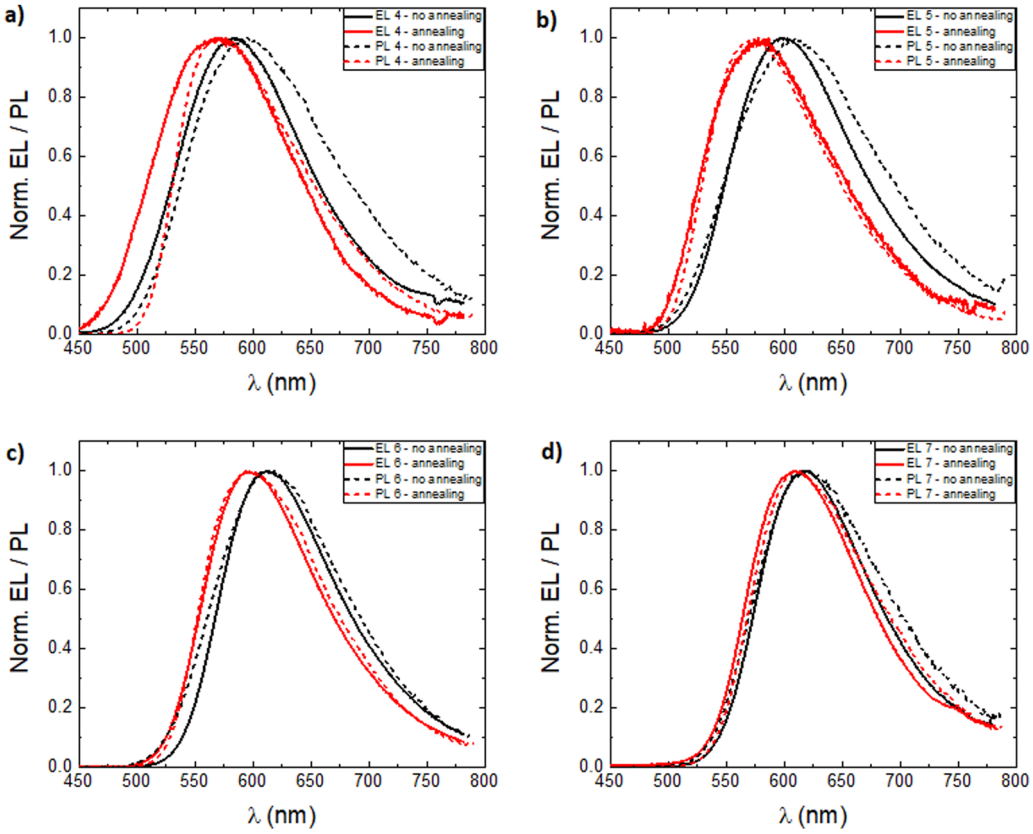

Fig. 7 Comparison between normalized electroluminescence and photoluminescence spectra using: (a) compound **4**; (b) compound **5**; (c) compound **6**; (d) compound **7**, before and after thermal annealing.

particular, devices with molecules **4**, **5**, **6** and **7** dispersed in mCP show a maximum current efficiency of 2.8, 3.4, 6.4 and 7.6 cd A^{-1}, respectively, with luminance that in any case exceeds 1000 cd m^{-2}. Conversely, self-quenching induces detrimental effects on neat film-based devices, for which the performance drops considerably, both in terms of efficiency and luminance. This behaviour is even more evident if the neat film EMLs are annealed after deposition. In that case, although the quantum yield is higher in modified films than in amorphous films (Table 2), we found that OLEDs exposed to the annealing step (and thus also exhibiting aggregation/crystallisation in the EML) generally have much lower efficiencies (see Fig. 6). This may be due to alterations in the morphology of the active layer as a result of heat exposure and the induced supramolecular organisation, which negatively impacts the electrical characteristics of the devices to a greater extent than any increase in PLQY. This also emerges from the current density curves as a function of the applied voltage, where it is clear that in the case of devices with an annealed EML there is a significant increase in passive currents even at low voltage. The external quantum efficiency (EQE) has been estimated for all OLEDs and is shown in Fig. S41 (ESI†).

We then compared the electroluminescence spectra of the devices with an EML in neat film (Fig. 7), with and without thermal annealing. The latter was used to induce/accelerate an eventual transition from the amorphous phase of the film to an aggregate/crystalline phase, as was observed in optical studies of the corresponding films. In all devices exposed to annealing at 150 °C, a shift of the emission towards higher energies can be observed, compared to the spectra of the non-annealed devices. The shift is in line with that observed in the steady-state photoluminescence spectra (Table 2) and suggests the formation of aggregates or crystalline domains whose optical properties are also reflected in electroluminescence.

2.5. MCL study

Building on the observation that these materials can form optically and structurally distinct solid-state phases depending on the processing conditions, we also tested explicitly their MCL properties. All MCL studies were performed using the setup described in the ESI† (Fig. S42). Initial powders of **4**–**7** obtained from the synthesis appeared visually as either multicrystalline, or amorphous (Fig. S43–S46, ESI†). Firstly, these starting powders were subjected to mechanical stress (Fig. 8 and Fig. S47, ESI†) by grinding the materials with a pestle in a mortar. The powders were then exposed to vapours of DCM and toluene (in the order shown in Fig. 8 and Fig. S47, ESI†). To compare the different forms obtained in the films with the phases obtained in the MCL study, Table 4 reports the emission

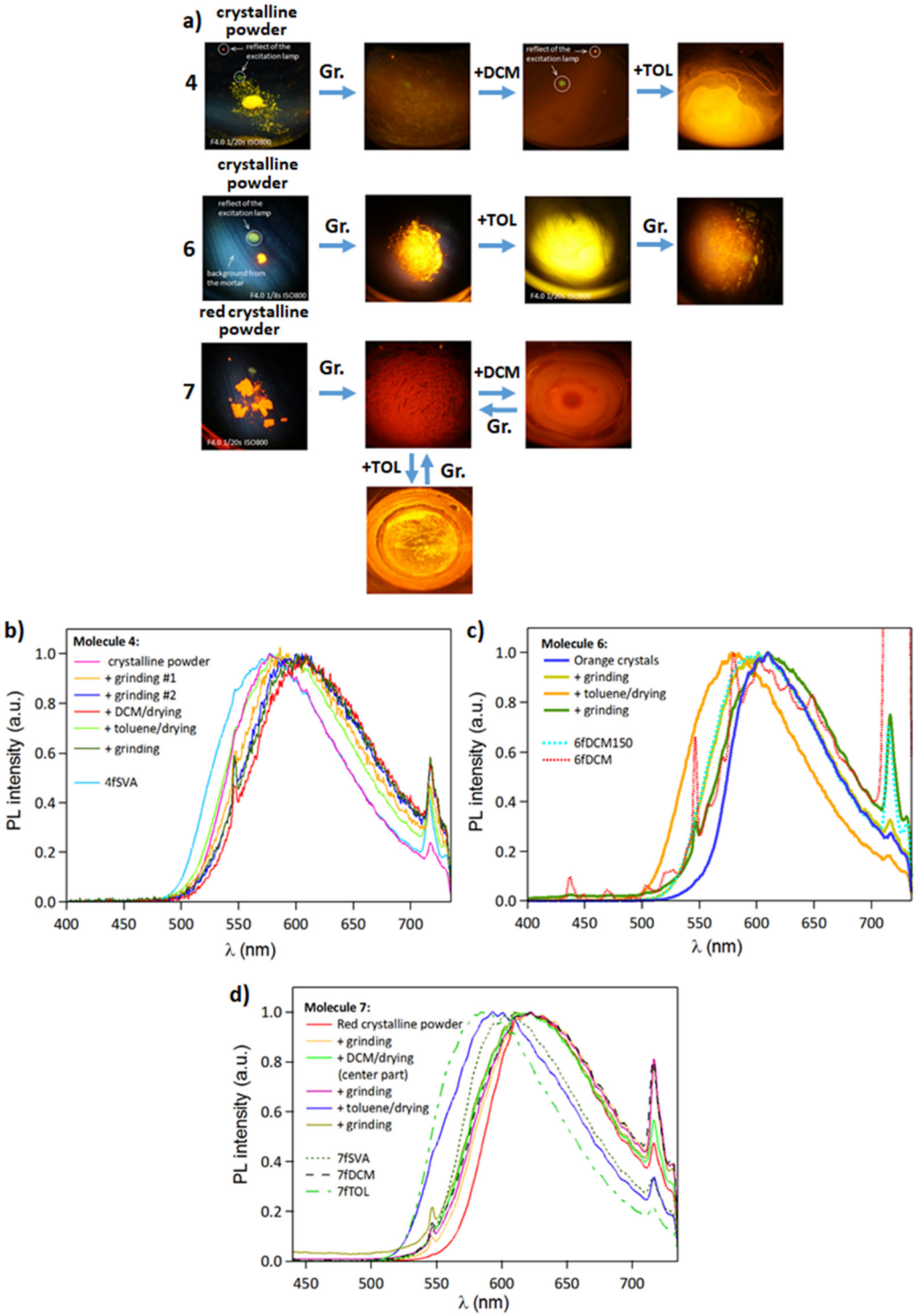

Fig. 8 MCL study for molecules **4**, **6** and **7**: (a) photographs of various forms obtained during the MCL study (the photographs were taken at 365 nm excitation); (b) PL spectra of the various forms of **4** studied in MCL, and PL spectra of **4fSVA** obtained with the MCL setup. (c) PL spectra of the various forms of **6** studied in MCL, and PL spectra of **6fDCM150** and **6fDCM** obtained with the MCL setup. (d) PL spectra of the various forms of **7** studied in MCL, and PL spectra of **7fSVA**, **7fDCM** and **7fTOL** obtained with the MCL setup. (Gr.: grinding; +TOL: exposition to toluene; +DCM: exposition to DCM).

maxima for the MCL study, while Table S5 (ESI†) shows the PL λ_{max} of the neat films. Table S5 (ESI†) also compares the PL obtained with the MCL setup to that obtained with the spectrofluorometer. It should be noted that the slight spectral shift in the latter case is due to the correction applied to the detector response, leaving the two setups still comparable.

Table 4 Emission maxima of the different phases obtained in the MCL study

	(Initial)[a] λ_{PL}, nm	+Grinding[b] λ_{PL}, nm	+DCM vapour[c] λ_{PL}, nm	+Grinding λ_{PL}, nm	+TOL vapour[d] λ_{PL}, nm	+Grinding λ_{PL}, nm
4 cryst. powd.	577	#1, 586 #2, 599	608	—	582	601
5 cryst. powd.	578	603	608	—	608	—
6 cryst-red powd.	629	611	610	—	609	—
6 orange cryst	610	601	—	—	578	610
7 crystal	602	624	—	—	—	—
7 red powder	621	621	621	621	592	621

[a] Initial powder. [b] Grinding in the mortar. [c] Exposure to DCM vapour. [d] Exposure to Toluene vapour.

The initial crystalline powders of compounds **4** (Fig. 8) and **5**§ (Fig. S47, ESI†) show a bright yellow emission similar to that of **4fSVA** and **5fSVA**. Upon grinding, the emission shifts to red and its brightness decreases, resulting in spectra similar to those of **4fDCM** and **5fDCM**, indicating the formation of amorphous phases also in the powders. The ground powders of **4** and **5** were then exposed to DCM vapours (+DCM), resulting in a slight red shift of the emission. Subsequent exposure to toluene vapours (+TOL) caused the emission to return to the initial position, similar to that of **4fTOL**, indicating the restoration of the crystalline form. However, no spectral shift was observed when **5** (+DCM) was exposed to toluene (+TOL) (Fig. S47, ESI†), consistent with the behaviour of **5fTOL**.

Two different forms of compound **6** were observed in the initial powder precipitated from the same batch (Fig. S45, ESI†). One form appeared as a polycrystalline red powder (Fig. S45 and S47, ESI†) with a narrow emission (λ_{max} = 629 nm) similar to both **6fSVA** and **6fDCM200** (steady state). The other form appeared as an orange crystal (λ_{max} = 610 nm) (Fig. 8 and Fig. S45, circled, ESI†). These two forms were manually separated with a pair of tweezers. Grinding of the polycrystalline red powder resulted in a broadened and blue-shifted emission (18 nm), indicating the formation of an amorphous phase with emission similar to that of **6fDCM**. Grinding of the orange crystals (Fig. 8) resulted in a blue shift (9 nm) together with broadening of the emission. The compound remained crystalline as indicated by the emission matching with **6fDCM150** (Fig. 8c). Finally, exposure of the ground orange crystal to toluene resulted in a hypsochromic shift (23 nm) with a narrowed yellow emission, different from that observed for the drop-cast thin films, indicating the formation of a possible additional polymorph that red-shifts upon grinding.

The initial powder of compound **7** also presented two different forms (Fig. S46, ESI†): one as a multicrystalline orange powder (λ_{max} = 601 nm, Fig. S47, ESI†) and the other as a red powder (λ_{max} = 621 nm, Fig. 7). Grinding the multicrystalline orange powder (similar emission to **7fSVA**, Fig. S47, ESI†) resulted in a red-shifted emission similar to **7fDCM**, indicating the formation of the amorphous phase. Grinding the red powder (Fig. 8) resulted in a blue-shift of the emission onset, which becomes broader and similar to that of **7fDCM**, indicating that the initial powder contained a more ordered phase. Exposure of the ground powder to DCM did not change the emission, consistent with an amorphous material. Finally, exposure to toluene favoured crystallisation, as indicated by the strong blue shift (λ_{max} = 592 nm), matching that of **7fTOL**. A second grinding redshifted the emission back to the amorphous phase.

Overall, the MCL behaviour observed for compounds **4–7** can be rationalized by considering both intramolecular conformational flexibility and supramolecular organization, as revealed by single-crystal XRD, thin-film XRD, and SEM analyses. The D–A torsion angles extracted from the single-crystal data (Table S1, ESI†) vary between polymorphs and influence the electronic coupling between donor and acceptor moieties, thus modulating the energy and efficiency of the CT excited states. Crystalline samples such as **fSVA** derivatives (excluding **6fSVA**), **6fDCM150**, and **7fTOL** exhibit blue-shifted, narrower, and more intense emission consistent with more twisted D–A conformations and reduced non-radiative decay. This behaviour is likely due to conformational locking and restricted relaxation pathways in ordered molecular environments. In contrast, red-shifted and broader emission with lower PLQYs, as observed for **6fSVA**, **6fDCM200**, **5fTOL**, and the amorphous **fDCM** samples, is indicative of more planar D–A conformations and enhanced CT stabilization. While in amorphous films this behaviour is likely due to increased conformational freedom, in crystalline samples such as **6fSVA** and **6fDCM200**, it likely arises from polymorph-specific packing that favours less twisted conformations and promotes non-radiative decay, in line with the energy gap law. SEM analysis of both **6fSVA** and **6fDCM200** confirms the presence of well-defined crystalline domains, excluding morphological disorder as the origin of their red-shifted and low-efficiency emission. This further supports the hypothesis that specific polymorphs with more planarized D–A geometries are responsible for enhanced CT stabilization and reduced radiative efficiency, highlighting the complex role of molecular packing in governing excited-state behaviour. SEM analysis of the thin films (Fig. 3 and Fig. S11, ESI†) provides direct insight into their surface morphology. Crystalline samples (**fSVA**, **fTOL**, **fDCM150**) with their long-range molecular order correlate with higher PLQYs and more structured emission. Conversely, amorphous films (**fDCM**, **5fTOL**) appear smooth and featureless, reflecting disordered packing and reduced emission efficiency. Although SEM was

§ Since **5** has similar emission properties to **4**, MCL experiments are described in the ESI.†

not performed on ground powders, the correlation observed in thin films provides a structural framework to interpret the emission shifts seen in MCL experiments (Fig. 8 and S47, ESI†). Mechanical grinding induces amorphization, allowing conformational relaxation and red-shifted emission. Recrystallization *via* solvent vapor exposure restores surface order and blue-shifted emission, as seen in **fSVA**, **fTOL**, and **fDCM150** samples.

Together, these results demonstrate a strong correlation between surface morphology, molecular packing, and emission properties, confirming that both intramolecular torsion and supramolecular organization govern the reversible MCL behaviour of these materials.

3. Experimental section

3.1. Photophysical setup

Absorption spectra were collected using a Cary 4000 double beam spectrophotometer (Agilent). Luminescence spectra were collected on a FluoroLog3 fluorescence spectrometer (Horiba Jobin Yvon). The relative photoluminescence quantum yields in solution were determined from corrected emission spectra using quinine dication (Φ_{PL} = 0.59 in $HClO_4$)[40] as the standard. The photoluminescence quantum yield of the films was measured by an absolute method with a barium sulphate-coated integrating sphere F-3018(Horiba) inserted into the spectrofluorimeter sample compartment. Fluorescence (PF and DF) and phosphorescence spectra and decays in the solid state (PMMA, neat film) were recorded by nanosecond gated luminescence and lifetime measurements (from 400 ps to 1 s) using either third harmonics of a high-energy, pulsed Nd:YAG laser emitting at 355 nm (EKSPLA) or a N2 laser emitting at 337 nm. Emission was focused onto a spectrograph and detected on a sensitive gated iCCD camera (Stanford Computer Optics) of subnanosecond resolution. PF/DF time-resolved measurements were performed by exponentially increasing gate and delay times. Lifetimes were extracted by a multi-exponential mathematical fit.

3.2. Film processing

(a) Doped PMMA films casting: all blends were obtained by drop-casting DCM solutions (0.1 g L^{-1}) of the compounds at room temperature on quartz slides followed by slow (1 night) evaporation in solvent saturated conditions. Concentration of the fluorophore in the film is reported in weight percentage (w/w) relative to the polymer mass in the solution. All blends formed clear, glassy, transparent solid films.

(b) Neat films were obtained by:

– Solvent vapour annealing (SVA): a few drops of a toluene solution containing the material are deposited onto a quartz substrate, which is placed on a support inside a glass container. This container has a small amount of hexane (approximately one finger's depth) at the bottom, below the support. The film is exposed to the vapours of the organic solvents, causing it to swell as the vapours penetrate it. This swelling allows the molecules within the film to become more mobile and reorganize. As the solvent evaporates, the film solidifies into a crystalline morphology. The degree of reorganization depends on factors such as the type of solvent, the duration of exposure, and the temperature.

– Drop-casting from solutions: in this process, a small amount of a solution containing the desired material is deposited onto the quartz substrate. The solvent is then allowed to evaporate, leaving behind a uniform thin film of the material. Key factors that influence the quality of the film include the concentration of the solution, the nature of the solvent, the substrate surface properties, and the evaporation conditions such as temperature and humidity.

– Thermal annealing: the material, in the form of a thin film is heated to a specific temperature below its melting point and maintained at that temperature for a set period. This heat treatment allows the material's atoms or molecules to move and rearrange, reducing defects and promoting crystallinity. Key parameters that affect the annealing outcome include the annealing temperature, duration, and cooling rate.

(c) Polycrystalline powders: as synthesized powders were collected from the PE/DCM solution.

3.3. XRD analysis

X-ray diffraction data for compounds **4** & **6** were collected by using a VENTURE PHOTON100 CMOS Bruker diffractometer with Micro-focus IuS source Cu Kα (for compound **6**) and Mo Kα (for compound **4**) radiation. X-ray diffraction data for compounds **5** & **7** were collected by using a Kappa X8 APPEX II Bruker diffractometer with graphite-monochromated Mo Kα radiation (=0.71073 Å). For more information see the ESI† section of *J. Phys. Chem. B* 2022, **126**, 2740–2753.[31]

3.4. Scanning electron microscopy (SEM) measurements

The samples were mounted on standard SEM stubs and subsequently transferred into the microscope chamber for imaging. SEM analyses were performed using a Carl Zeiss high-resolution field emission SEM (FE-SEM) SIGMA 300VP, equipped with GEMINI® column technology. Images were acquired using both the in-lens secondary electron (SE) detector and the angle-selective backscattered electron (HBSD) detector. Measurements were conducted under high vacuum and variable pressure (VP) conditions, with nitrogen used as the imaging gas to enable analysis of non-conductive specimens without the need for conductive coatings.

3.5. OLED devices

The OLED device structure was as follow: ITO/Pedot:PSS AI 4083 (35 nm)/PVK (polyvinylcarbazole – average $M_w \approx$ 1 100 000)/EML/TPBI (2,2′,2″-(1,3,5-benzinetriyl)-tris(1-phenyl-1-*H*-benzimidazole))/LiF (1 nm)/Al (100 nm). We tested 3 different EMLs: molecules (**4**, **5**, **6**, and **7**) were dispersed in 1,3-bis(*N*-carbazolyl)benzene (mCP) at 20% w/w, 100% neat film of molecule, and 100% annealed neat film. Pedot:PSS was spin coated at 2500 rpm for 60 s (35 nm). PVK was dissolved in chloroform:chlorobenzene (95 : 5 v/v), 3 mg ml^{-1}, and then spin coated at 8000 rpm for 60 s (10 nm). Materials **4**

and **5** were dissolved in toluene (10 mg ml^{-1}), while 6 and 7 in dichloromethane : chlorobenzene (60 : 40 relative v/v ratio, 10 mg ml^{-1}). mCP was dissolved in chlorobenzene (20 mg ml^{-1}) and then properly mixed with the molecule solutions to obtain final concentrations of 10 mg ml^{-1} for all formulations. All the EMLs were deposited by spin coating at 1500 rpm for 60 s (30 nm). Finally, TPBI (50 nm), LiF (1 nm) and Al (100 nm) were thermally evaporated in a high vacuum chamber (1×10^{-6} mbar).

3.6. Mechanochromic luminescence setup

The study of mechanochromism was performed using the simple setup shown in Fig. S1 (ESI†). The sample was placed inside a ceramic mortar and the emission was collected before and after grinding the sample with a pestle. As an excitation source an Hg–Xe Lamp (Lightningcure LC8 from Hamamatsu), coupled to an optic fibre, equipped with an appropriate interferential filter to select the 365 nm Hg line, was used. Another fiber was used to detect the emission and sent to a CCD camera. The emission spectra were recorded by a CCD-based spectrograph QEPro from Ocean Optics.

4. Conclusions

In summary, we demonstrate the ability to control the supramolecular arrangement of a series of D–A–D materials by varying the chemical and physical processing conditions. X-ray diffraction shows the ability of the compounds to pack in different polymorphs in the obtained neat films, giving tuneable emission and TADF properties correlated with the different molecular conformations. OLED devices using annealed emissive layers show similar trends in electroluminescence, arising from the formation of amorphous and crystalline phases as seen in the photophysical measurements. Finally, we show that the materials exhibit reversible and multistage mechanoluminescence properties under external stimuli, which is again correlated with the presence of different polymorphs/aggregates observed in the neat films. The design and study of new materials such as these allows tuning of solid-state luminescence properties with both MCL and TADF activity, enabling future applications in optoelectronic devices such as pressure and volatile organic vapour sensors.

Data availability

The data supporting this article have been included as part of the ESI.†

Conflicts of interest

There are no conflicts to declare.

Acknowledgements

The research leading to these results has received funding from the European Union's Horizon 2020 research and innovation program under the Marie Skłodowska-Curie grant agreement number 674990 (EXCILIGHT). This work was also supported by the Italian Ministry of Research (MUR) under the complementary actions to the NRRP (PNC0000007) "Fit4MedRob-Fit for Medical Robotics" Grant (contract number CUP B53C22006960001). Arnaud Brosseau is acknowledged for his technical support in the PPSM laboratory (ENS-Paris Saclay).

References

1 O. Ostroverkhova, Organic Optoelectronic Materials: Mechanisms and Applications, *Chem. Rev.*, 2016, **116**(22), 13279–13412.
2 W. C. H. Choy, W. K. Chan and Y. P. Yuan, Recent Advances in Transition Metal Complexes and Light-Management Engineering in Organic Optoelectronic Devices, *Adv. Mater.*, 2014, **26**(31), 5368–5399.
3 G. J. Hedley, A. Ruseckas and I. D. W. Samuel, Light Harvesting for Organic Photovoltaics, *Chem. Rev.*, 2017, **117**(2), 796–837.
4 H. Kaji, H. Suzuki, T. Fukushima, K. Shizu, K. Suzuki, S. Kubo, T. Komino, H. Oiwa, F. Suzuki, A. Wakamiya, Y. Murata and C. Adachi, Purely organic electroluminescent material realizing 100% conversion from electricity to light, *Nat. Commun.*, 2015, **6**, 8476.
5 Y. J. Cho, B. D. Chin, S. K. Jeon and J. Y. Lee, 20% External Quantum Efficiency in Solution-Processed Blue Thermally Activated Delayed Fluorescent Devices, *Adv. Funct. Mater.*, 2015, **25**(43), 6786–6792.
6 H. Uoyama, K. Goushi, K. Shizu, H. Nomura and C. Adachi, Highly efficient organic light-emitting diodes from delayed fluorescence, *Nature*, 2012, **492**(7428), 234–238.
7 F. B. Dias, K. N. Bourdakos, V. Jankus, K. C. Moss, K. T. Kamtekar, V. Bhalla, J. Santos, M. R. Bryce and A. P. Monkman, Triplet Harvesting with 100% Efficiency by Way of Thermally Activated Delayed Fluorescence in Charge Transfer OLED Emitters, *Adv. Mater.*, 2013, **25**(27), 3707–3714.
8 M. Montrone, A. Maggiore, A. Moliterni, P. Pander, M. Pugliese, A. L. Capodilupo, S. Gambino, C. T. Prontera, V. Valenzano, F. Mariano, G. Accorsi, T. Sibillano, C. Giannini, G. Gigli, A. Cardone and V. Maiorano, New [1]benzothieno[3,2-b]benzothiophene-tetraoxide-based TADF emitters with a D–A–D structure for OLED applications, *J. Mater. Chem. C*, 2025, **13**(1), 160–176.
9 F. B. Dias, J. Santos, D. R. Graves, P. Data, R. S. Nobuyasu, M. A. Fox, A. S. Batsanov, T. Palmeira, M. N. Berberan-Santos, M. R. Bryce and A. P. Monkman, The Role of Local Triplet Excited States and D-A Relative Orientation in Thermally Activated Delayed Fluorescence: Photophysics and Devices, *Adv. Sci.*, 2016, **3**(12), 1600080.
10 Q. S. Zhang, H. Kuwabara, W. J. Potscavage, S. P. Huang, Y. Hatae, T. Shibata and C. Adachi, Anthraquinone-Based Intramolecular Charge-Transfer Compounds: Computational Molecular Design, Thermally Activated Delayed

Fluorescence, and Highly Efficient Red Electroluminescence, *J. Am. Chem. Soc.*, 2014, **136**(52), 18070–18081.

11 H. Tanaka, K. Shizu, H. Nakanotani and C. Adachi, Twisted Intramolecular Charge Transfer State for Long-Wavelength Thermally Activated Delayed Fluorescence, *Chem. Mater.*, 2013, **25**(18), 3766–3771.

12 Y. N. Hong, J. W. Y. Lam and B. Z. Tang, Aggregation-induced emission: phenomenon, mechanism and applications, *Chem. Commun.*, 2009, 4332–4353.

13 Y. Q. Dong, J. W. Y. Lam, A. J. Qin, Z. Li, J. Z. Sun, H. H. Y. Sung, I. D. Williams and B. Z. Tang, Switching the light emission of (4-biphenylyl)phenyldibenzofulvene by morphological modulation: crystallization-induced emission enhancement, *Chem. Commun.*, 2007, 40–42.

14 J. S. Ward, A. Danos, P. Stachelek, M. A. Fox, A. S. Batsanov, A. P. Monkman and M. R. Bryce, Exploiting trifluoromethyl substituents for tuning orbital character of singlet and triplet states to increase the rate of thermally activated delayed fluorescence, *Mater. Chem. Front.*, 2020, **4**(12), 3602–3615.

15 L. Salah, M. K. Etherington, A. Shuaib, A. Danos, A. A. Nazeer, B. Ghazal, A. Prlj, A. T. Turley, A. Mallick, P. R. McGonigal, B. F. E. Curchod, A. P. Monkman and S. Makhseed, Suppressing dimer formation by increasing conformational freedom in multi-carbazole thermally activated delayed fluorescence emitters, *J. Mater. Chem. C*, 2021, **9**(1), 189–198.

16 A. Maggiore, Y. Qu, P. Pander, F. B. Dias, G. Clavier, R. Guillot, D. Altamura, C. Giannini, V. Maiorano, P. Audebert and F. Miomandre, Sonocrystallization induced thermally activated delayed fluorescence *via* distortion of molecular geometry, *J. Mater. Chem. C*, 2024, **12**(22), 7943–7955.

17 A. Maggiore, X. Tan, A. Brosseau, A. Danos, F. Miomandre, A. P. Monkman, P. Audebert and G. Clavier, Novel D–A chromophores with condensed 1,2,4-triazine system simultaneously display thermally activated delayed fluorescence and crystallization-induced phosphorescence, *Phys. Chem. Chem. Phys.*, 2022, **24**(29), 17770–17781.

18 Y. Q. Dong, J. W. Y. Lam and B. Z. Tang, Mechanochromic Luminescence of Aggregation-Induced Emission Luminogens, *J. Phys. Chem. Lett.*, 2015, **6**(17), 3429–3436.

19 S. Yagai, T. Seki, H. Aonuma, K. Kawaguchi, T. Karatsu, T. Okura, A. Sakon, H. Uekusa and H. Ito, Mechanochromic Luminescence Based on Crystal-to-Crystal Transformation Mediated by a Transient Amorphous State, *Chem. Mater.*, 2016, **28**(1), 234–241.

20 Y. Sagara and T. Kato, Mechanically induced luminescence changes in molecular assemblies, *Nat. Chem.*, 2009, **1**, 605.

21 Z. G. Chi, X. Q. Zhang, B. J. Xu, X. Zhou, C. P. Ma, Y. Zhang, S. W. Liu and J. R. Xu, Recent advances in organic mechanofluorochromic materials, *Chem. Soc. Rev.*, 2012, **41**(10), 3878–3896.

22 Z. Y. Ma, Z. J. Wang, M. J. Teng, Z. J. Xu and X. R. Jia, Mechanically Induced Multicolor Change of Luminescent Materials, *Chem. Phys. Chem.*, 2015, **16**(9), 1811–1828.

23 Y. Sagara, S. Yamane, M. Mitani, C. Weder and T. Kato, Mechanoresponsive Luminescent Molecular Assemblies: An Emerging Class of Materials, *Adv. Mater.*, 2016, **28**(6), 1073–1095.

24 P. P. Yu, Y. G. Zhen, H. L. Dong and W. P. Hu, Crystal Engineering of Organic Optoelectronic Materials, *Chem*, 2019, **5**(11), 2814–2853.

25 D. Liu, C. G. Li, S. J. Niu, Y. Li, M. X. Hu, Q. Y. Li, W. G. Zhu, X. T. Zhang, H. L. Dong and W. P. Hu, A case study of tuning the crystal polymorphs of organic semiconductors towards simultaneously improved light emission and field-effect properties, *J. Mater. Chem. C*, 2019, **7**(20), 5925–5930.

26 M. M. Li, A. H. Balawi, P. J. Leenaers, L. Ning, G. H. L. Heintges, T. Marszalek, W. Pisula, M. M. Wienk, S. C. J. Meskers, Y. P. Yi, F. Laquai and R. A. J. Janssen, Impact of polymorphism on the optoelectronic properties of a low-bandgap semiconducting polymer, *Nat. Commun.*, 2019, 10.

27 A. Maggiore, M. Pugliese, F. Di Maria, G. Accorsi, M. Gazzano, E. Fabiano, V. Tasco, M. Esposito, M. Cuscuna, L. Blasi, A. Capodilupo, G. Ciccarella, G. Gigli and V. Maiorano, Exploiting Photo- and Electroluminescence Properties of FIrpic Organic Crystals, *Inorg. Chem.*, 2016, **55**(13), 6532–6538.

28 P. Data and Y. Takeda, Recent Advancements in and the Future of Organic Emitters: TADF- and RTP-Active Multifunctional Organic Materials, *Chem.– Asian J.*, 2019, **14**(10), 1613–1636.

29 R. Pashazadeh, P. Pander, A. Lazauskas, F. B. Dias and J. V. Grazulevicius, Multicolor Luminescence Switching and Controllable Thermally Activated Delayed Fluorescence Turn on/Turn off in Carbazole-Quinoxaline-Carbazole Triads, *J. Phys. Chem. Lett.*, 2018, **9**(5), 1172–1177.

30 M. Okazaki, Y. Takeda, P. Data, P. Pander, H. Higginbotham, A. P. Monkman and S. Minakata, Thermally activated delayed fluorescent phenothiazine-dibenzo a,j phenazine-phenothiazine triads exhibiting tricolor-changing mechanochromic luminescence, *Chem. Sci.*, 2017, **8**(4), 2677–2686.

31 A. Maggiore, Y. Y. Qu, R. Guillot, P. Pander, M. Vasylieva, P. Data, F. B. Dias, P. Audebert, G. Clavier and F. Miomandre, Novel Easy to Synthesize Benzonitrile Compounds with Mixed Carbazole and Phenoxazine Substituents Exhibiting Dual Emission and TADF Properties, *J. Phys. Chem. B*, 2022, **126**(14), 2740–2753.

32 M. Aydemir, S. D. Xu, C. J. Chen, M. R. Bryce, Z. G. Chi and A. P. Monkman, Photophysics of an Asymmetric Donor-Acceptor-Donor′ TADF Molecule and Reinterpretation of Aggregation-Induced TADF Emission in These Materials, *J. Phys. Chem. C*, 2017, **121**(33), 17764–17772.

33 G. De Luca, E. Treossi, A. Liscio, J. M. Mativetsky, L. M. Scolaro, V. Palermo and P. Samori, Solvent vapour annealing of organic thin films: controlling the self-assembly of functional systems across multiple length scales, *J. Mater. Chem.*, 2010, **20**(13), 2493–2498.

34 T. Seki, Y. Takamatsu and H. Ito, A Screening Approach for the Discovery of Mechanochromic Gold(I) Isocyanide

Complexes with Crystal-to-Crystal Phase Transitions, *J. Am. Chem. Soc.*, 2016, **138**(19), 6252–6260.

35 J. Wu, Y. Cheng, J. Lan, D. Wu, S. Qian, L. Yan, Z. He, X. Li, K. Wang, B. Zou and J. You, Molecular Engineering of Mechanochromic Materials by Programmed C–H Arylation: Making a Counterpoint in the Chromism Trend, *J. Am. Chem. Soc.*, 2016, **138**(39), 12803–12812.

36 M. K. Etherington, N. A. Kukhta, H. F. Higginbotham, A. Danos, A. N. Bismillah, D. R. Graves, P. R. McGonigal, N. Haase, A. Morherr, A. S. Batsanov, C. Pflumm, V. Bhalla, M. R. Bryce and A. P. Monkman, Persistent Dimer Emission in Thermally Activated Delayed Fluorescence Materials, *J. Phys. Chem. C*, 2019, **123**(17), 11109–11117.

37 H. T. Sun, Z. B. Hu, C. Zhong, X. K. Chen, Z. R. Sun and J. L. Bredas, Impact of Dielectric Constant on the Singlet-Triplet Gap in Thermally Activated Delayed Fluorescence Materials, *J. Phys. Chem. Lett.*, 2017, **8**(11), 2393–2398.

38 J. T. Ye, L. Wang, H. Q. Wang, X. M. Pan, H. M. Xie and Y. Q. Qiu, Effective Impact of Dielectric Constant on Thermally Activated Delayed Fluorescence and Nonlinear Optical Properties: Through-Bond/-Space Charge Transfer Architectures, *J. Phys. Chem. C*, 2018, **122**(33), 18850–18859.

39 G. Haykir, M. Aydemir, A. Tekin, E. Tekin, A. Danos, F. Yuksel, G. Hizal, A. P. Monkman and F. Turksoy, Effects of donor position and multiple charge transfer pathways in asymmetric pyridyl-sulfonyl TADF emitters, *Mater. Today Commun.*, 2022, **31**, 103550.

40 C. Würth, M. Grabolle, J. Pauli, M. Spieles and U. Resch-Genger, Relative and absolute determination of fluorescence quantum yields of transparent samples, *Nat. Protoc.*, 2013, **8**(8), 1535–1550.